Recent Advances in Compressive Sensing for Production Test and Antenna Diagnostics of 5G Massive MIMO Antennas

C.G. Parini[1],
[(1)] Queen Mary University of London,
London, Mile End Road,
E1 4NS, UK

S.F. Gregson[1,2]
[(2)] Next Phase Measurements,
11521 Monarch St, Garden Grove,
CA, USA

***Abstract*—In this paper we introduce a novel technique for the efficient production test and measurement of 5G, Massive MIMO array antennas for the purpose of verification, diagnostics, and fault detection that drastically reduces the number of measurements required and the associated acquisition time needed. The technique utilises compressive sensing and sparse sampling combined with a total variation measurement approach that enforces the requisite sparsity on the problem. In this paper, we compare this new spherical near-field total-variation based acquisition approach with the authors existing, analogous, planar technique. Extensive performance comparisons are presented which aggregate results across many test cases which is a necessity, and a consequence of the statistical nature of the compressive sensing technique that is imposed by virtue of the requirements of the Restricted Isometry Property (RIP). Crucially, this paper identifies and addresses a fundamental flaw within the application of many total-variation based methods and especially when used with the difference field between a reference antenna and a production test antenna. This extends the use of a novel analysis process that incorporates an l_0 based minimisation strategy to overcome this problem thereby restoring the CS process to very nearly the levels of performance attained in our prior work.**

I. INTRODUCTION

Compressive Sensing (CS) and Sparse Sampling based techniques [1, 2, 3, 4] have been deployed in a variety of free-field metrology-based applications including radar imaging [5], cylindrical [6] and spherical near-field measurements [7, 8], far-field reflection suppression [9], and for array antenna measurement and diagnostics [10, 11, 12, 13]. For the case of Massive MIMO antenna measurements, CS has been successfully used to reduce the number of measurements needed to verify the antenna array's excitation in a production test environment [14, 15, 16, 17] assuming failure rates of typically less than 5%. These have largely followed the general approach of creating the sparsity needed by CS through an application of the total variation method which involves subtracting the measured far-field, or near-field, of the assumed defective production test array antenna from that of a known reference "gold-standard" antenna when acquired under identical conditions [10, 11, 12, 13].

In prior papers by the authors [16, 17], the basic concept of the CS based planar near-field (PNF) array diagnostics using the equivalent currents (EC) method can be found described in detail. To summarise the method, we first exploit the fact that the 'gold' reference antenna exists and explore the use of CS to undertake a back propagation to the antenna's aperture from the PNF measurement of the *difference* between the NF pattern of the AUT, and the 'gold' antenna using minimal, randomly located, NF measurements. Here, the intention is to minimise the number of measurement points, M, required to accurately and reliably measure the antenna in the PNF, whilst accurately reconstructing the array antenna's radiating element excitations. However, in this paper, and in contrast to prior works in this area of application, here, the NF is assumed to have been acquired using a spherical acquisition geometry.

The structure of this paper is as follows. Section II presents an overview of the EC method which here is extended to admit the generalised spherical geometry and its associated polarisation. Section III provides an introduction to the CS technique which is more complex than that which has been treated previously as it accommodates each of the individually measured polarisations simultaneously. Section IV presents a verification of the SNF EC based aperture diagnostics formulation which underpins the new total-variation CS technique, before Section V presents a comparison of the planar and spherical CS implementations. Section VI presents an examination of the effect of electrical path length difference between probe and gold standard antenna and that of probe to test antenna which can pose a fundamental limitation in the creation of the total-variation difference pattern. Lastly, Section VII contains a summary and the conclusions.

II. OVERVIEW OF THE SNF EC METHOD

A detailed treatment of the EC method for planar acquisition geometries can be found in the open literature [15, 16, 17] thus, for the sake of brevity, we shall herein only consider the extension to the related spherical case. As is widely known, the equivalent magnetic current approach utilises a Green's function based formulation to obtain an equivalent magnetic current sheet over a convenient surface that encloses the AUT from the electromagnetic (EM) field acquired across a two-dimensional surface in front of the radiator. Once the equivalent currents (EC) have been determined, they can be used to propagate the electric fields elsewhere in space, including out to the far-field [15]. In this procedure, an electric field integral equation (IE) is constructed which relates the measured near electric fields to a set of equivalent magnetic currents which can be solved using an efficient, but resource intensive, method of moments (MoM) procedure [15, 18]. This typically involves a point

matching technique which converts the IE into an equivalent linear algebra, *i.e.* matrix, form allowing it to be solved in one of several ways, *e.g.* by determining the Moore-Penrose pseudoinverse, or from the least squares conjugate gradient (LSQR) method [15, 18], the latter being as popular choice.

Let us assume that the radiator is placed in the back half-space and is radiating forward into the positive half-space, with the two regions bounded by an infinitely large *xy*-plane. If we introduce an infinite perfect electric conducting (PEC) sheet on one side of the surface, then in this case only the tangential components of the electric fields need be specified over that surface. Thus, for an antenna with a well-defined aperture, by using the image theorem, the magnetic currents can be expressed to a good approximation as [15, 18, 19],

$$\underline{J_m}(\underline{r'}) = \begin{cases} 2\left(\underline{E_a}(\underline{r'}) \times \underline{\hat{n}}\right) & \text{over the aperture,} \\ 0 & \text{elsewhere.} \end{cases} \tag{1}$$

The electric vector potential $\underline{F}$ may be defined in terms of the integral of this equivalent current sheet as [15, 18, 19],

$$\underline{F}(\underline{r}) = \frac{\varepsilon}{4\pi}\int_S \frac{\underline{J_m}(\underline{r'})}{R} e^{-jk_0 R} ds' \tag{2}$$

Here, primed variables are used to represent the source point, whilst un-primed variables are associated with the field point. The free-space propagation constant is denoted by k_0, and the displacement R can be expressed as,

$$R = |\underline{r} - \underline{r'}| = \sqrt{(x-x')^2 + (y-y')^2 + (z-z')^2} \tag{3}$$

Since we can obtain the electric fields from the electric vector potential $\underline{F}$ using [3, 15, 18],

$$\underline{E}(\underline{r}) = -\frac{1}{\varepsilon}\left(\nabla' \times \underline{F}(\underline{r'})\right) \tag{4}$$

Then by exchanging the order of integration and differentiation we may write that,

$$\underline{E}(\underline{r}) = -\frac{1}{4\pi}\int_S \nabla' G(\underline{r}, \underline{r'}) \times \underline{J_m}(\underline{r'})\, ds' \tag{5}$$

Here, $\underline{J_m}$ denotes the surface magnetic current sheet that we seek, $G(r,r')$ is the Greens function, and $\underline{E}(\underline{r})$ is the electric field that is measured across the SNF measurement surface S, which is located at a radius that is more than a few wavelengths from the AUT to insure it is outside of the reactive NF [15]. If we assume a spherical coordinate system and polarisation basis, then we may write this in a more convenient linear algebra form as [15, 18, 19],

$$\begin{bmatrix} E_x(r_0,\theta,\phi) \\ E_y(r_0,\theta,\phi) \\ E_z(r_0,\theta,\phi) \end{bmatrix} = \frac{-1}{4\pi}\int_S \begin{bmatrix} 0 & \frac{\partial G}{\partial z} & \frac{\partial G}{\partial y} \\ -\frac{\partial G}{\partial z} & 0 & \frac{\partial G}{\partial x} \\ \frac{\partial G}{\partial y} & -\frac{\partial G}{\partial x} & 0 \end{bmatrix} \cdot \begin{bmatrix} J_{mx}(x',y') \\ J_{my}(x',y') \\ J_{mz}(x',y') \end{bmatrix} ds' \tag{6}$$

Here we employ the field equivalence principle [15] to represent the field at an arbitrary point in space as an integral over the surface on which the fields are known where the free-space Green's function can be expressed as,

$$G(r,r') = \frac{e^{-jk_0|\underline{r}-\underline{r'}|}}{|\underline{r}-\underline{r'}|} \tag{7}$$

Here, the partial derivatives of G are,

$$\frac{\partial G}{\partial x} = \frac{e^{-jk_0 R}}{R^2}(x-x')\left(jk_0 + \frac{1}{R}\right) \tag{8}$$

$$\frac{\partial G}{\partial y} = \frac{e^{-jk_0 R}}{R^2}(y-y')\left(jk_0 + \frac{1}{R}\right) \tag{9}$$

$$\frac{\partial G}{\partial z} = \frac{e^{-jk_0 R}}{R^2}(z-z')\left(jk_0 + \frac{1}{R}\right) \tag{10}$$

Since the cartesian and spherical fields can be related [15],

$$\begin{bmatrix} E_\theta \\ E_\phi \\ E_r \end{bmatrix} = \begin{bmatrix} \cos\theta\cos\phi & \cos\theta\sin\phi & -\sin\theta \\ -\sin\phi & \cos\phi & 0 \\ \sin\theta\cos\phi & \sin\theta\sin\phi & \cos\theta \end{bmatrix} \cdot \begin{bmatrix} E_x \\ E_y \\ E_z \end{bmatrix} \tag{11}$$

Combining this into a single block-Toeplitz form yield,

$$\begin{bmatrix} E_\theta(\underline{r}) \\ E_\phi(\underline{r}) \\ E_r(\underline{r}) \end{bmatrix} = \frac{-1}{4\pi}\int_S \begin{bmatrix} H_{1,1} & H_{1,2} & H_{1,3} \\ H_{2,1} & H_{2,2} & H_{2,3} \\ H_{3,1} & H_{3,2} & H_{3,3} \end{bmatrix} \cdot \begin{bmatrix} J_{mx}(\underline{r'}) \\ J_{my}(\underline{r'}) \\ J_{mz}(\underline{r'}) \end{bmatrix} ds' \tag{12}$$

Recognising that the EC method only requires the measurement of the tangential field components on the SNF surface allows us to rewrite (12) as:

$$\begin{bmatrix} E_\theta(\underline{r}) \\ E_\phi(\underline{r}) \end{bmatrix} = \frac{-1}{4\pi}\int_S \begin{bmatrix} H_{1,1} & H_{1,2} & H_{1,3} \\ H_{2,1} & H_{2,2} & H_{2,3} \end{bmatrix} \cdot \begin{bmatrix} J_{mx}(\underline{r'}) \\ J_{my}(\underline{r'}) \\ J_{mz}(\underline{r'}) \end{bmatrix} ds' \tag{13}$$

Where,

$$H_{1,1} = -\frac{\partial G}{\partial z}\cos\theta\sin\phi - \frac{\partial G}{\partial y}\sin\theta \tag{14}$$

$$H_{1,2} = \frac{\partial G}{\partial z}\cos\theta\cos\phi + \frac{\partial G}{\partial x}\sin\theta \tag{15}$$

$$H_{1,3} = -\frac{\partial G}{\partial y}\cos\theta\cos\phi + \frac{\partial G}{\partial x}\cos\theta\sin\phi \tag{16}$$

$$H_{2,1} = -\frac{\partial G}{\partial z}\cos\phi \tag{17}$$

$$H_{2,2} = -\frac{\partial G}{\partial z}\sin\phi \tag{18}$$

$$H_{2,3} = \frac{\partial G}{\partial y}\sin\phi + \frac{\partial G}{\partial x}\cos\phi \tag{19}$$

This integral equation can be solved using a method of moments (MoM) approach [15, 18, 19] which involves us utilising the sampling theorem to replace the continuous current sheet with an array of fictitious magnetic dipoles, and the electric fields with a set of discrete samples. This is equivalent to using a Dirac delta function for the expansion of the current sources, and enables us to replace the integration with a summation with the resulting system of equations,

$$[E] = [H][J_m] \tag{20}$$

This is block-Toeplitz in form, thus each of the $H_{n,m}$ sub-matrices have $n_{\text{measurements}}$ rows, by n_{currents} columns resulting in the complex matrix $[H]$ comprising $3\times n_{\text{measurements}}$ rows by $2\times n_{\text{currents}}$ columns in all, which will rapidly become computationally and resource intensive. Similarly, the column vector $[E]$ contains all the measured points for all of the

individual polarisations and thus will have $2\times n_{measurements}$ rows and one column with $[J_m]$ being a column vector with $3\times n_{currents}$ rows and a single column. Thus, the coefficients for the fictitious magnetic dipole array can be obtained by solving this system of linear equations [15, 18, 19]. Crucially, and as will be discussed in the next section, this system of equations is in a form that is amenable for tackling with CS.

III. Overview of Compressive Sensing

In this section we provide a brief introduction to sparse sampling and CS. CS is a way of sampling signals in the knowledge the signals are sparse in some given domain. Classically, when expressed in a linear algebra form, we would say that as we have fewer equations than unknowns, then there are an infinite number of solutions. However, we can still find a solution to an underdetermined linear system of equations on the condition that the solution is sparse, *i.e.* that most of the elements are zero. To do this however, the method requires incoherent measurements, *i.e.* randomness, where the number of measurements required depends on the sparsity of the final solution. It is only in the last fifteen years or so that advances in applied mathematics and statistics have allowed us to solve this efficiently and robustly for the sparsest [s]. This process can be seen summarized in Figure 1 below, where we wish to construct the full NF (x) from a small number of samples (y) via a transform domain (ψ) with sparse coefficients (s).

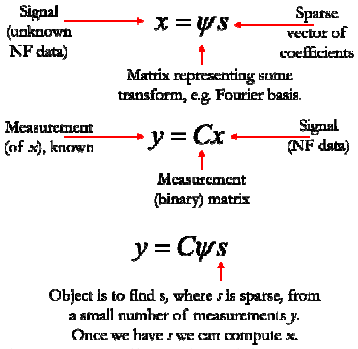

Figure 1. Illustration of the CS concept.

To illustrate the CS problem, we consider the task of finding s, where s is sparse, from a small number of incoherent measurements y that satisfy the restricted isometry property (RIP) [10]. Thus, we find s by optimizing,

$$\min \|S\|_1 \text{ s.t. } \|y - C\psi s\|_2 < \sigma \tag{21}$$

Here, C needs to be incoherent with respect to ψ, *i.e.* as far away from $C = \psi^{-1}$ as is possible and the term σ is determined by the noise level within the measurement. In our case y denotes sample NF measurements, C is the measurement matrix which defines the NF sample point locations, and ψ represents the transform from element current to NF point. As noted above, a comprehensive discussion of the CS principle is beyond the scope of this paper however, more information is available in the open literature, *e.g.* [10]. To efficiently solve (21), several software packages are available, *e.g.* CVX [20], YALL1 [21], and SPGL1 [22] which are all readily accessible. For this study, we have chosen to utilize the YALL1 algorithm due to its efficiency and accuracy [15].

IV. Verification of SNF EC Method

We first consider a conventional spherical near-field scan of a 20 x 28 element dipole array with half wavelength spacing and operating at 8.2GHz. Here we have included four randomly located faults to this array of the form -6dB and 45°; -10dB and -75°; -30dB and 135°; -3dB and 110° which can be seen presented in Figure 2 below.

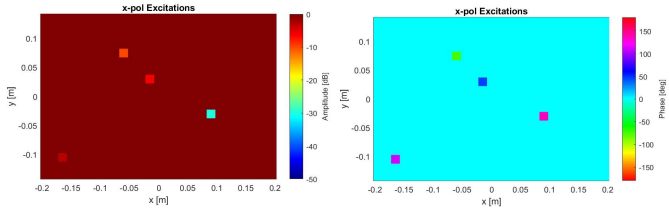

Figure 2. Elemental element excitations of the 8.2 GHz planar array antenna, amplitude left, phase right.

We then simulate a standard SNF acquisition of this defective planar array antenna shown in Figure 3 (a), (b) below.

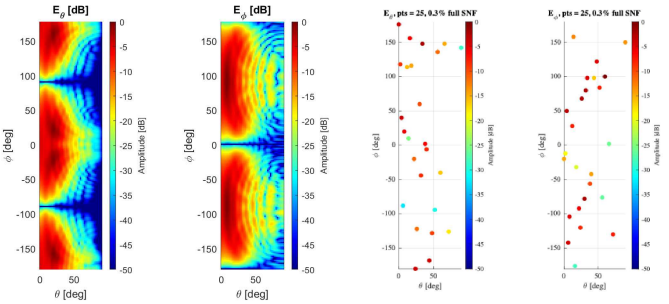

Figure 3. Simulated SNF E_θ (a), E_ϕ (b) amplitudes, Sparse sampled E_θ (c), E_ϕ (d) locations and amplitudes.

Here, the hemi-spherical measurement surface places the NF probe at a distance of 10λ at 8.2 GHz as measured from the centre of the aperture of the antenna, which is just 2% of the classical FF distance [15] and includes measurement noise level set at -60dB from the peak signal level. This measurement had 8280 points in all and complied with the standard spherical near-field sampling theorem [15]. Using the method developed above in Section III, we may then compute the equivalent magnetic current across the surface of the array's aperture and see the amplitude and phase of the equivalent currents of the defective array as shown in Figure 4.

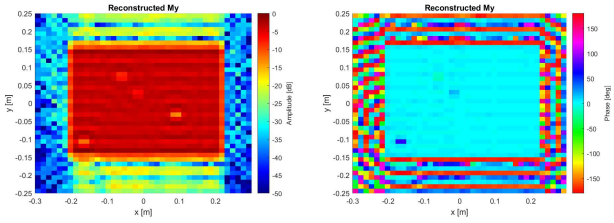

Figure 4. Reconstructed amplitude left, phase right.

Here, from observation, we can see that the positions of the defective elements have been recovered correctly. As is often the case with such moment-method type reconstructions, some stray fields are evident outside of the antenna aperture. In general, it has been noted that the results are improved when the correct location of the radiating elements is used within the reconstruction of the equivalent surface currents. This can be taken to provide encouraging confirmation of the effectiveness of the underlying EC spherical measurement technique. In the

next section results of an exhaustive comparison between the planar [16, 17] and new spherical CS approach can be seen.

V. Comparison of PNF & SNF CS Results

As CS is inherently a statistical process, we must run each of the respective CS algorithms a larger number of time and aggregate the results. For this example, we used 25 NF samples of an 8 x 24 element rectangular planar array 5G Massive MIMO base station antenna, with 4 amplitude and phase faults included each at -1dB, and ±22°.

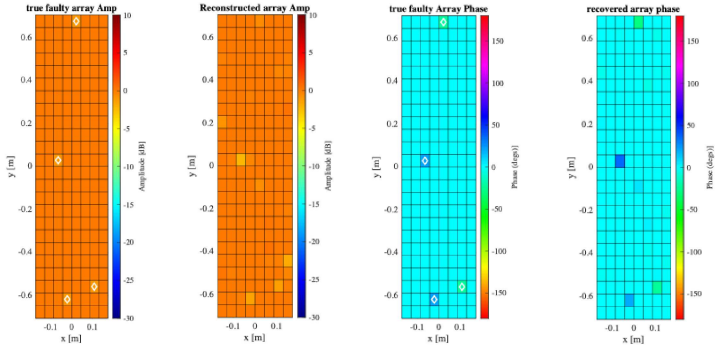

(a) (b) (c) (d)

Figure 5. Comparison of element amplitude (a) and (b) and phase (c) and (d) excitations, and CS reconstructed excitations (b) and (d) from PNF measurements.

A typical reconstruction result is: amplitude and phase at (3, 7) =-1.3 dB, -23.8°, with a target =-1 dB, -22°, amplitude and phase at (13, 3) =-2.2 dB, 35.3°, with a target =-1 dB, 22°, amplitude and phase at (24, 5) =-0.6 dB, -28.6°, with a target =-1 dB, -22°, and lastly, amplitude and phase at (2, 4) =-1.5 dB, 20.8°, with a target =-1 dB, 22°. The result for one case can be seen presented in Figure 5, which shows comparisons of the elemental excitations and the reconstructed elemental amplitude and phase excitations where the location of the faulty elements are highlighted by the white diamonds. As in our previous work, we use a statistical measure of reconstruction performance based on plotting the cumulative distribution function (CDF) [14] of the RMS error of the reconstructed array amplitude excitation over 50 runs for different fault locations and look at the statistics of the reconstruction [16, 17]. This can be seen presented in Figure 6 where Blue is rms reconstruction error over all array elements, Red is Maximum rms error over all array, Yellow is rms reconstruction error over faulty array elements.

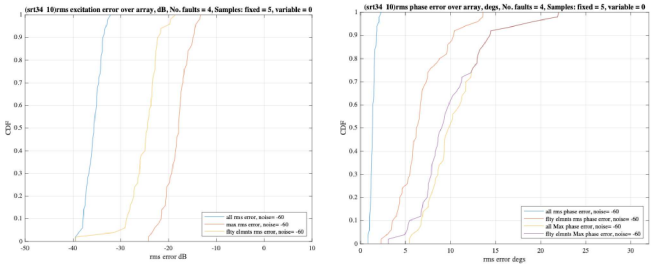

Figure 6. CDF of CS reconstructed excitations for 50 runs of different sample points, amplitude left, phase right.

Next, we can repeat this using the equivalent spherical implementation. Figure 3 (c) and (d) shows the SNF samples that were used in one run of the CS processing. Here, the coloured dots represent the location and amplitude of the samples. Again, a typical reconstruction is: excitation at 20,2, true: amp =-1dB, phase=-22°, recovered: amp =-0.7dB, phase=-14.4°, excitation at 10,4, true: amp = -1dB, phase= 22°, recovered: amp =-1.0 dB, phase= 20.5°, excitation at 8,8, true: amp = -1dB, degs= -22°, recovered: amp =-0.7dB, phase= -19.3°, excitation at 13,3, true: amp = -1dB, phase= 22°, recovered: amp =-0.6dB, phase= 31.4°. As for the PNF case, the result for one SNF case can be seen in Figure 7, which present comparisons of the elemental excitations and the reconstructed elemental amplitude and phase excitations. As we did for the planar case above, we plotted the CDF of the RMS error of the reconstructed array amplitude excitation over 50 runs for different locations for the faults. This can be seen presented in Figure 8 below which may be directly compared with the planar case of Figure 6 above.

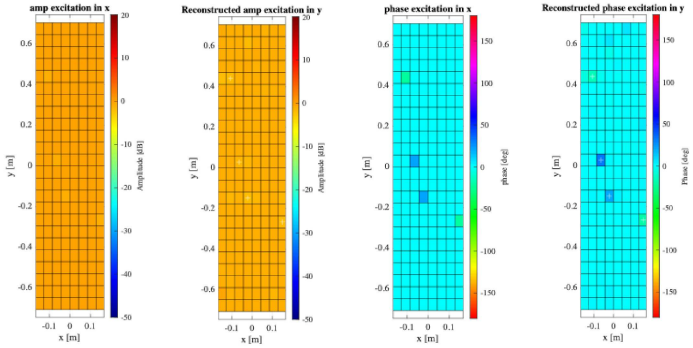

(a) (b) (c) (d)

Figure 7. Comparison of element amplitude (a) and (b) and phase (c) and (d) excitations, and CS reconstructed excitations (b) and (d) from SNF measurements.

If we take the 80% CDF MSE level as a useful reference point to compare results of the 50 runs (*i.e.* 80% of the runs will be better than or equal to this MSE value) and look at the statistics of the reconstruction we see that for the planar case, all RMS amplitude error at CDF of 0.68 and 0.8 (dB) =-34.9, -34.2 respectively, and for the equivalent spherical case, all RMS amplitude error at CDF of 0.68 and 0.8 (dB) =-34.1, -33.4.

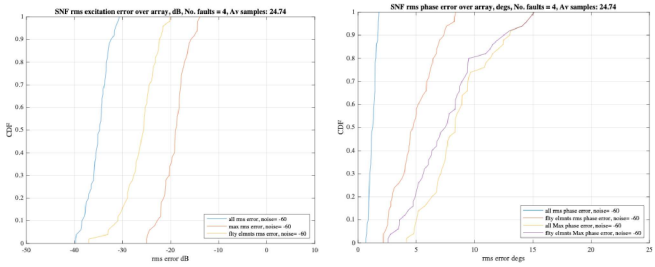

Figure 8. Comparison of amplitude element excitations, and CS reconstructed excitations, *cf.* Fig. 6.

VI. Electrical Pathlength Error & Mitigation

The use of CS in array diagnosis is predicated on measuring the NF difference between the gold antenna and the antenna under test (AUT). In practice this must entail the NF measurement of the gold antenna at the 25 sample points and then the placing of the AUT in *exactly the same* location to measure the same 25 NF samples. We thus need to understand the tolerance of the CS process to both transverse location errors (x,y) between the gold and AUT antennas as well as the longitudinal (z) ones. For a $x = y = 0.01\lambda = 0.9$mm transverse

translation of the AUT with respect to the gold antenna, we found an acceptably small level of performance degradation. For a longitudinal (z) location error of 0.01λ the corresponding 80% CDF all element rms reconstruction error drops from -28.3 dB to a poor -21.1 dB. Clearly the tolerance to longitudinal alignment of the CS measurement system is *much* more critical than that of transverse alignment. This result is not surprising when we realise that any z translation between gold and AUT antennas is effectively a phase change across the AUT array, so every element has effectively a phase fault added to it, rendering the system non-sparse. Even if one could engineer a mechanical alignment system that could be accurate to within 0.17mm (0.002λ = 0.7°), such a phase change could be easily generated by RF subsystem thermal drift between the NF acquisition of gold and AUT. As far as the authors are aware this problem has not been highlighted before in the open literature. To overcome this z-tolerance issue, we have proposed and verified through simulation the following scheme:

- Count cells of the reconstructed array with amplitude < ± 1 dB of the known gold array excitation and assume there is no error on these cells.
- Similarly, count cells of the reconstructed array phase < ± 5° of the known gold array excitations and assume there is no error on these cells.
- Plot these values as a scan through various values of z deflection are tried in the CS code over a range of z = ± 0.05λ with a step size of 0.0025λ.
- Pick the set that has the largest count (*i.e.* minimum number of faulty elements) to give an estimate of the true z error.

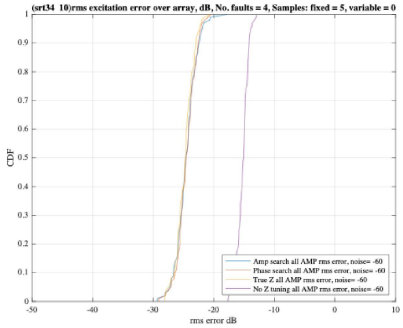

Figure 9. CDF rms amplitude reconstruction error for z-location error process (25 samples 4 randomly located faults) taken over 50 sets of different fault locations. Gold to AUT misaligned in z by 0.03λ

Figure 9 shows the CDF rms amplitude reconstruction error for the above z-location error process when repeated 100 times with 25 fixed samples, and 4 randomly located faults. Shown on this figure are the CDF results for the following cases of reconstructing the array excitations using: the z-location error detected using the amplitude counts (blue); the z-location error detected using the phase counts (red); the true value of z-location error (0.03λ in this case) (yellow); the case with no attempt at z-location error correction (magenta). Clearly, the recovery process works correctly with both amplitude and phase detected error corrections having identical results to the true z-error case. It is worth noting from Fig.10 that there is a 10dB degradation in performance when no z-location error correction is employed.

VII. Summary & Conclusions

This paper has presented a novel, total-variation based, spherical CS technique for production array antenna diagnostics that can be used for the test of electrically large antennas. We have obtained very similar levels of performance for the existing planar and new spherical implementations. The performance analysis for the specific massive MIMO array considered here suggests that fault levels up to *circa* 2% can be identified confidently, with performance degrading as the number of faults increase and hence as the problem becomes progressively less sparce. Depending upon the level of reconstruction accuracy required, we have found that arrays with up to 4% element failure rate are suitable for this CS based diagnostics with this level of failure being greater than what could be expected to be encountered in a typical massive MIMO array production line. Lastly, in applying the total-variation based CS technique for practical array diagnosis through measurement simulation and undertaking a tolerance study, we have identified the longitudinal alignment tolerance required between the *gold* reference antenna as being a crucial consideration for the successful deployment of the approach. We have proposed and verified through simulation a l_0 based optimisation routine being successfully harnessed to recover a *circa* 10 dB improvement in the amplitude reconstruction error that returns much of the original systems performance.

References

[1] D.L. Donoho, "Compressed sensing," in *IEEE Trans. Inf. Theory*, vol. 52, no. 4, Apr. 2006

[2] E. J. Candes and T. Tao, "Near-optimal signal recovery from random projections: universal encoding strategies?" IEEE Transactions on Information Theory, vol. 52, no. 12, pp. 5406–5425, Dec. 2006. 2, 40.

[3] E. J. Candes, J. Romberg, and T. Tao, "Robust uncertainty principles: Exact signal reconstruction from highly incomplete frequency information," IEEE Transactions on Information Theory, vol. 52, no. 2, pp. 489–509, 2006. 2, 39,40.

[4] S. Foucart and H. Rauhut, A mathematical introduction to compressive sensing. Springer, 2013.

[5] L. C. Potter, E. Ertin, J. T. Parker, and M. Cetin, "Sparsity and compressed sensing in radar imaging," Proc. IEEE, vol. 98, no. 6, pp. 1006–1020, 2010.

[6] M. Salucci, M. D. Migliore, P. Rocca, A. Polo and A. Massa, "Reliable antenna measurements in a near-field cylindrical setup with a sparsity promoting approach," *IEEE Trans. Antennas Propag.*, vol. 68, no. 5, pp. 4143-4148, May 2020

[7] R. Cornelius, D. Heberling, N. Koep, A. Behboodi and R. Mathar, "Compressed sensing applied to spherical near-field to far-field transformation," in *Proc. European Conf. Antennas Propag. (EuCAP),* Davos, Switzerland, 2016, pp. 1-4.

[8] C. Culotta-López and D. Heberling, "Fast spherical near-field measurements on arbitrary surfaces by application of pointwise probe correction to compressed sampling Schemes," *in Proc. Antenna Measurement Techniques Association Symposium (AMTA),* San Diego, CA, USA, 2019, pp. 1-6

[9] Z. Chen, S.F. Gregson, Y. Wang, "Novel Application of Compressed Sensing in Cylindrical Mode Filtering for Far-Field Antenna Measurements", Antenna Measurement Techniques Association Annual Symposium, October 2023, Seattle, USA.

[10] M. D. Migliore, "A compressed sensing approach for array diagnosis from a small set of near-field measurements," *IEEE Trans. Antennas Propag.*, vol. 59, no. 6, pp. 2127–2133, Jun. 2011.

[11] B. Fuchs and M. D. Migliore, "Array diagnosis from far field data via ℓ1 minimizations," *Proc. European Conf. Antennas Propag. (EuCAP),* The Hague, Netherlands, 2014, pp. 1239-1242

[12] B. Fuchs, L. L. Coq, and M. D. Migliore, "Fast antenna array diagnosis from a small number of far-field measurements," *IEEE Trans. Antennas Propag.*, vol. 64, no. 6, pp. 2227–2235, Jun. 2016.

[13] B. Fuchs, L. Le Coq, S. Rondineau, and M. D. Migliore, “Compressive sensing approach for fast antenna far field characterization,” in 12th European Conference on Antennas and Propagation (EuCAP). IEEE, 2018. 3, 42, 48

[14] S.F. Gregson, Z. Qin, C.G. Parini, “Compressive Sensing in Massive MIMO Array Testing: A Practical Guide”, IEEE Transactions on Antennas and Propagation, 2022, Volume: 70, Issue: 9

[15] S.F. Gregson, J. McCormick, C.G. Parini, “Principles of Planar Near-Field Antenna Measurements, 2nd Edition”, IET Electromagnetic Waves series 53, ISBN 978-1-83953-699-1, July 2023.

[16] C.G. Parini, S.F. Gregson, “Compressive Sensing Applied to Planar Near-Field Based Array Antenna Diagnostics for Production Testing”, AMTA 2023, October 2023, Seattle, USA.

[17] C.G. Parini, S.F. Gregson, “Compressive Sensing Applied to Production Testing of Array Antennas using a Robotic Arm and Very Sparsely Sampled Near-Field Measurements”, 18th European Conference on Antennas and Propagation (EuCAP), 17-22 March 2024, Glasgow, Scotland.

[18] C. G. Parini, S. F. Gregson, J. McCormick, D. Janse van Rensburg, T.S. Eibert, “Theory and Practice of Modern Antenna Range Measurements”, (2nd expanded edition), IET Press, 2020, in 2 volumes, ISBN 978-1-83953-126-2 and ISBN 978-1-83953-128-6.

[19] T.K. Sarkar, M. Salazar-Palma, M.D. Zhu, H. Chen, “Modern Characterization of Electronic Systems and its Associated Metrology”, IEEE Press, 2021, ISBN 978-1-119-07646-9.

[20] Michael Grant and Stephen Boyd, “CVX: Matlab Software for Disciplined Convex Programming, Version 2.0 beta,” http://cvxr.com/cvx, last accessed September 2013.

[21] YALL1 basic solver code: Y. Zhang, J. Yang, and W. Yin. Available for download from https://github.com/andrewssobral/YALL1, last accessed 4th July 2024.

[22] E. van den Berg and M. P. Friedlander, “SPGL1: A Solver for Large-scale Sparse Reconstruction”, https://friedlander.io/spgl1/, last accessed December 2019.